Bessel beam beating-based spontaneous Raman tomography enables high-contrast deep tissue Raman measurements

Zhiwei Huang (biehzw@nus.edu.sg)
National University of Singapore https://orcid.org/0000-0002-0104-9135
Chi Shu
National University of Singapore
Li Gong
National University of Singapore

Article

Keywords: spontaneous Raman tomography, Bessel beam beating, deep Raman spectroscopy

Posted Date: October 28th, 2022

DOI: https://doi.org/10.21203/rs.3.rs-2041850/v1

Additional Declarations: (Not answered)

Bessel beam beating-based spontaneous Raman tomography enables high-contrast deep tissue Raman measurements

Chi Shu[1], Li Gong[1], Zhiwei Huang[1]*

Affiliations:

[1] Optical Bioimaging Laboratory, Department of Biomedical Engineering, College of Design and Engineering, National University of Singapore, Singapore 117576

* **Correspondence to:**

Dr. Zhiwei Huang, Optical Bioimaging Laboratory, Department of Biomedical Engineering, College of Design and Engineering, National University of Singapore, 9 Engineering Drive 1, Singapore 117576

Tel: +65- 6516-8856

Fax: +65- 6872-3069

E-mail: biehzw@nus.edu.sg

Running title: Spontaneous Raman tomography for deep tissue Raman measurements

Keywords: spontaneous Raman tomography, Bessel beam beating, deep Raman spectroscopy

Abstract

We report on the development of a novel Bessel beam beating-based spontaneous Raman tomography (B^3-SRT) technique for depth-resolved deep tissue Raman characterization without a need of mechanical depth-scan. To accomplish B^3-SRT, we conceive a unique method by designing a coaxial Bessel beam beating excitation scheme associated with the Bessel beam collection configuration, such that the depth-resolved Raman information is encoded by the Bessel beam beatings generated, and then the depth-encoded Raman spectra along the Bessel beam excitation region are collected simultaneously by a Bessel-shaped collection optical designed. The depth-resolved Raman spectra can be rapidly retrieved using inverse fast Fourier transform. We demonstrated the ability of B^3-SRT technique for high contrast deep tissue Raman measurements in a highly scattering two-layer tissue phantom (e.g., fat-bone tissue model). Compared with conventional confocal Raman microscopy, B^3-SRT provides ~3.7-fold improvement in deep tissue Raman detection as well as ~2.6-fold improvement in deeper bone tissue Raman spectral contrast in the highly scattering fat-bone tissue phantom. It is anticipated that B^3-SRT technique developed has potential to facilitate high contrast depth-resolved deep tissue Raman measurements in biomedical systems.

Introduction

Raman spectroscopy is a vibrational spectroscopy technique capable of unravelling the biomolecular fingerprint information about the samples,[1,2] which has been widely used for label-free cell and tissue biomolecular characterization (e.g., disease diagnosis,[3–6] and cancer treatment follow-ups[7]). The conventional spontaneous Raman spectroscopy is usually utilized to probe the Raman signal from surface and/or subsurface of the sample without axial sectioning ability.[8,9] Confocal Raman spectroscopy uses a pinhole placed in front of the detector to achieve the axial tissue optical sectioning by rejecting the out-of-focus scattered tissue Raman signals in tissue.[10] Due to the inherent strong scattering nature of tissue, the excitation laser propagation in tissue is largely attenuated and the out-of-focus Raman photons could be scattered back to the collection pin hole in confocal Raman spectroscopy measurements. Consequently, the axial sectioning and Raman excitation/collection capability of confocal Raman spectroscopy are dramatically deteriorated, particularly in deep tissue Raman measurements.[8,11–14] To tackle the challenges, several deep Raman spectroscopy methods (e.g., spatially offset Raman spectroscopy (SORS), and Kerr-gating Raman spectroscopy (KRS)).[8,15,16] have been introduced mostly based on the photon migration theory where the Raman signal originating from deeper tissue layer shows differences in spatial domain due to the encountering of more scattering processes compared to Raman signal from shallower tissue layers.[8] Due to the stochastic scattering processes, current deep Raman spectroscopy techniques with solving the inverse problem can only provide the depth-resolved Raman spectra with an axial resolution of~ mm scale.[8,17] Meanwhile, the tissue Raman spectra collected using photon migration-based deep Raman spectroscopy techniques are unpreventably contaminated by the Raman signals arising from other tissue layers, the Raman spectrum unmixing algorithms (e.g., over-constrained library-based fitting method) are usually utilized for these deep Raman techniques to enhance the quality of deep tissue Raman spectra.[18] The development of more advanced deep tissue Raman spectroscopy techniques with high axial sectioning capability is highly desirable for further understanding of biomolecular structures and conformation in deep tissue from turbid biological/biomedical systems.

In this work, we present a novel Bessel beam beating-based spontaneous Raman tomography (B^3-SRT) technique enabled by a unique Bessel beam beating excitation and Bessel collection scheme conceived for high contrast deep tissue Raman measurements with micron-scale resolution. In B^3-SRT, the sample is illuminated by the excitation Bessel beam beatings generated to encode the axial information in the Raman signals. The depth-information encoded Raman signal is collected along the axial axis by using the uniquely designed Bessel collection optical system to effectively suppress the Bessel beam side lobe artefacts. The Hessian denoising algorithm is employed to effectively reduce the shot noise interference on the collected tissue Raman spectra. The depth-resolved Raman spectral information can be rapidly retrieved though inverse fast Fourier transform (IFFT) for deep tissue Raman characterization without a need of mechanical z-scan. We have derived and analyzed the working principle of the B^3-SRT technique theoretically, and also experimentally demonstrated its utility for high contrast deep tissue Raman measurements in a highly scattering fat-bone tissue phantom.

Working principle of B^3-SRT technique

In B^3-SRT, we employ a pair of superimposed optical Bessel beams designed with a spatial light modulator (SLM) to generate optical beatings along the z-direction for tissue excitation. The electric field of both optical Bessel beams can be described by using the 0^{th}-order Bessel function of the first kind (i.e., $J_0(r \cdot k_r)$ and $J_0(r \cdot k_r')$, where k_r and k_r' are the transverse wavevectors of the corresponding Bessel beams. The intensity profile of the excitation Bessel beam beating $I_{ex}(r,z)$ can be written as:

$$I_{ex}(r,z) = I_{ex}(z)\left|J_0(r \cdot k_r)e^{ik_z z} + J_0(r \cdot k_r')e^{i(k_z')z}\right|^2$$

$$= I_{ex}(z)[\left(J_0(r \cdot k_r)\right)^2 + \left(J_0(r \cdot k_r')\right)^2 + 2\cos(\Delta k_z z) J_0(r \cdot k_r) J_0(r \cdot k_r')], \quad (1)$$

where k_z and k_z' are the axial wavevectors of the superimposed Bessel beam pair, and Δk_z denotes the axial wavevector difference of the Bessel beams (i.e., $\Delta k_z = k_z - k_z'$). The cosine term in Eq. (1) (i.e., $\cos(\Delta k_z z)$) depicts the optical beating along the z axis. The beating frequency of the beating term is

controlled by both Δk_z and z, suggesting the possibility of encoding the depth information through manipulating a set of Bessel beam beatings with different Δk_zin B^3-SRT technique.[19]

To detect the beating term in the generated Raman signal, we further introduce a unique Bessel-shaped collection function $I_{co}(r,z) = I_{ac}(z)\left|J_0(r \cdot k_r'')\right|^2$ in B^3-SRT. The acquired Raman signal from a thin layer sample at the depth z_0 can be written as (Detailed derivations refer to **Supplemental S.1**):

$$I_{Ra}(\omega) \propto 2\pi f(\omega) I_{ex}(z_0) \int [\left(J_0(r \cdot k_r)\right)^2 + \left(J_0(r \cdot k_r')\right)^2 + 2\cos(\Delta k_z z_0) J_0(r \cdot k_r) J_0(r \cdot k_r')] |J_0(r \cdot k_r'')|^2 r dr$$

$$= 2\pi f(\omega) I_{ex}(z_0) [C + 4\pi \cos(\Delta k_z z) \iiint \frac{\delta(\left|\overrightarrow{k_r} + \overrightarrow{k_r'} + \overrightarrow{k_r''}\right| - \left|\overrightarrow{k_r''}\right|)}{k_r''} d\varphi d\varphi' d\varphi''] \quad (2)$$

where $\overrightarrow{k_r} = k_r(\cos\varphi + sin\varphi)$, $\overrightarrow{k_r'} = k_r'(\cos\varphi' + sin\varphi')$, and $\overrightarrow{k_r''} = k_r''(\cos\varphi'' + sin\varphi'')$, C is the direct current (DC) term. From Eq. (2), we observe that if there is a set of φ, φ' and φ'' allowing $\left|\overrightarrow{k_r} + \overrightarrow{k_r'} + \overrightarrow{k_r''}\right| = \left|\overrightarrow{k_r''}\right|$ to hold, the beating term $\cos(\Delta k_z z)$ can be reflected in the acquired Raman spectra $I_{Ra}(\omega)$. This requirement can be satisfied when k_r, k_r' and k_r'' obey the following condition:

$$|k_r - k_r'| \leq 2k_r'' \leq |k_r + k_r'|. \quad (3)$$

The generation of optical Bessel beam beating and the introducing of a Bessel-shaped collection function are further illustrated in **Figure 1(a)**. The excitation beating pattern generated by a pair of superimposed Bessel beam shows strong side lobes at the main lobe's troughs. The arising side lobes could also generate Raman signal as the Raman scattering is linearly proportional to the light intensity, resulting in the diminishment of beating in the collected Raman spectra. However, the Raman signal generated from the side lobes of the excitation beam can be effectively suppressed or eliminated by adding a unique Bessel-shaped collection function with specially designed k_r'' following the relationship stated in Eq. (3). As shown in **Figure 1(a)**, the final collected Raman signal using the Bessel-shaped collection function only contains the information from the main lobe of the excitation Bessel beam beating, allowing the simultaneous acquisition of the encoded beating information along z axis while eliminating the Bessel side lobe artefacts.

In B^3-SRT, the acquired Raman signal $I_{Ra}(\omega, \Delta k_z)$ of an object $f(\omega, z)$ excited by the Bessel beam beatings with different beating frequency Δk_z and collected by a Bessel-shaped collection function can be further illustrated from Eq. (2) as:

$$I_{Ra}(\omega, \Delta k_z) \propto \int_{-\infty}^{\infty} f(\omega, z)\, I_{ex}(z) I_{co}(z)[1 + \cos(\Delta k_z z)]\mathrm{d}z. \quad (4)$$

The depth information encoded in the acquired Raman spectra with the beating frequency Δk_z modulated ranging from $\Delta k_{z,min}$ to $\Delta k_{z,max}$ can be rapidly retrieved using an inverse Fast Fourier transform (IFFT):[19]

$$g(\omega, z') = \frac{1}{2\pi} \int_{\Delta k_{z,min}}^{\Delta k_{z,max}} I_{Ra}(\omega, \Delta k_z)\, e^{i\Delta k_z z'} \mathrm{d}\Delta k_z$$

$$= [f(\omega, z') I_{ex}(z') I_{co}(z') + f(\omega, -z') I_{ex}(-z') I_{co}(-z') + C_3 \delta(z')] * \frac{1}{2} sinc\left[\frac{(\Delta k_{z\,max} - \Delta k_{z\,min}) z'}{2}\right], \quad (5)$$

where $C_3 = 2\int_{-\infty}^{\infty} f(\omega, z)\, I_{ex}(z) I_{co}(z)$, $C\delta(z')$ is a delta function, and $*$ denotes convolution process. In Eq. (5), the first term $f(\omega, z') I_{ex}(z') I_{co}(z')$ represents the depth-resolved Raman spectra along the z-axis; the second term $f(\omega, -z') I_{ex}(-z') I_{co}(-z')$ represents the mirrored depth-resolved Raman spectra and the third term $C\delta(z')$ represents the direct current (DC) component. The axial resolution of B^3-SRT technique is controlled by the sinc function in Eq. (5), where the full width at half maximum (FWHM) of $\Delta z'$ is inverse proportional to $\Delta k_{z,max} - \Delta k_{z,min}$:[19]

$$\Delta z' = \frac{2.41\pi}{\Delta k_{z,max} - \Delta k_{z,min}}. \quad (6)$$

Figure 1(b) shows the workflow for retrieving the depth-resolved Raman spectra in B^3-SRT technique. The depth information is encoded into the Raman signal at different wavenumbers during Δk_z scanning, and thus without a need of mechanical z-scan, the depth-resolved Raman spectra can be rapidly retrieved through taking IFFT with respect to Δk_z on each Raman shift wavenumber. **Figure 1(c)** depicts the optical setup of B^3-SRT technique. The phase patterns are sequentially displayed on the SLM, generating a series of excitation Bessel beams with different spatial frequencies Δk_z. Each phase modulation pattern includes two concentric circular deflection patterns with different converging angles (**Figure 1(c)**), generating the two superimposed Bessel beams with different converging angles after

SLM.[19] The generated Raman signal is collected using a Bessel-shaped collection function achieved with an axicon-lens system designed (**Figure 1(c)**). An iris together with a long focal length lens (f = 200 mm in our study) is used in the collection optical path (**Figure 1(c)**), such that the MMF tip can be considered as a point detector (i.e., $r < \frac{0.61\lambda_{co}}{NA'}$, where r is the MMF core radius, λ_{co} is the collection photon wavelength and NA' is the collection numerical aperture at the MMF tip) (Detailed derivations for achieving Bessel collection refer to **Supplemental S.2**). From Eq. (4), we can observe that the plane $z = 0$ appears at the plane whose phase $\Delta k_z z$ is zero for all Δk_z. In current optical setup (**Figure 1(c)**), the plane $z = 0$ is the imaging plane of SLM where the excitation beam is modulated by the central pixel of the SLM which is always zero for all Δk_z. Meanwhile, only the beating patterns with $z \geq 0$ are generated by the SLM and projected onto the sample. Therefore, the B^3-SRT technique holds an advantage that the retrieved Raman spectra will never be overlapped with DC term and the mirrored spectra.[19]

Materials and Methods

Experimental Setup

The experimental setup of the B^3-SRT system is shown in **Figure 1(c)**. The excitation laser is provided by a 785 nm, single mode diode laser (Model: I0785SH0175B, maximum output power: 175 mW, IPS Lasers Inc.). The collimated excitation laser is then modulated into Bessel beam beatings using concentric axicon phase patterns on a SLM (SLM-200, santec Corporation). The modulated excitation Bessel beam beatings is then projected onto the sample through a 4-*f* system consists of a plano-convex lens (L1, f = 200 mm), a dichroic mirror (DM, Semrock) and a 20× Fluorite microscope objective (RMS20×-PF, NA = 0.5, Olympus). A band-pass laser filter (Semrock) is placed after L1 to eliminate the unwanted laser interference in the excitation beam. The Raman signal is collected by an axicon (AX251-B, physical angle: 1º, deflection angle: 0.5º, Thorlabs) and refocused by L3 to the tip of the multimode fiber (M105L02S-B, core diameter: 105 μm, low OH multimode fiber, Thorlabs). A long-pass filter (Semrock) is placed before L2 to remove the interference of excitation laser in the

Raman measurement. The collected Raman signal is then imaged using the Raman spectroscopy system consisting of a high-throughput reflective spectrograph (Acton LS-785 f/2, Princeton Instrumentation Inc.) equipped with a customized gold-coated 830 gr/mm grating and a near-infrared (NIR)-enhanced charge-coupled device (CCD) camera (PIXIS: 400BR-eXcelon, Princeton Instrumentation Inc.). The beam lengths for both the excitation Bessel beam and the collection distribution Bessel function generated are ~ 200 μm in the sample space. The single mode laser excitation power on the sample is ~ 80 mW. The confocal Raman spectroscopy measurement is achieved in the same optical setup by removing L2 and the axicon in the collection optical path and displaying a Fresnel lens phase pattern (f = 68 mm) on the SLM to focus the excitation beam on the sample. For B^3-SRT measurements, 51 phase patterns designed are sequentially displayed on the SLM and three Raman spectra are acquired within 60 s integration time for each phase pattern. For confocal Raman spectra measurement, the tissue sample is moved along z-axis with 5 μm step size. Three tissue Raman spectra are acquired with integration time of 10 s per spectrum at each depth.

Sample preparation

To assess the performance of B3-SRT technique in a highly scattering tissue model, we built a fat-bone tissue phantom. The porcine fat tissue and bone tissue samples used in the experiments are acquired from local market. The fat tissue is cut into the thickness of 50, 70 and 90 μm slides using Research Cryostat (CM3050, Leica). Then, the tissue phantom is prepared by covering the exposed bone (dimension: 5mm×5mm×2mm) with the fat slides of different thickness. The fat layer thickness of the prepared fat-bone tissue sample is further confirmed using optical coherence tomography (OCT) system (TEL320, Thorlabs). The optical properties of the fat and bone tissues at 785 nm are as follows: for the fat tissue- refractive index n of ~1.48, reduced scattering coefficient μ_s' of 14.3 cm^{-1}; for the bone tissue- refractive index n of 1.62, reduced scattering coefficient μ_s' of 17.6 cm^{-1}.[20,21] The poly(methyl methacrylate) (PMMA) sheet is used for axial resolution estimation (Material No. GF53167608, Sigma-Aldrich Pre Pte Ltd).

Data processing

The acquired Raman spectra are processed using the customized software developed on MATLAB (Mathworks Inc). Firstly, the spatial frequency domain Raman spectra $g(\omega, \Delta k_z)$ acquired with Bessel beam beatings of different Δk_z is smoothed in both wavenumber (ω) and spatial frequency (Δk_z) directions using customized two-dimensional Hessian denoising algorithm to suppress the random noise of the spectra (Detail refers to **Supplemental S.3**).[22] The fingerprint (FP) region (800 cm^{-1} – 1800 cm^{-1}) of the Raman spectra is then selected for the further processing. The autofluorescence (AF) background of the acquired spectra are removed using iterative polynomial fitting method with a fifth-order polynomial function.[4,5,7] The depth-resolved Raman spectra is rapidly retrieved by applying IFFT on each wavenumber of the spatial frequency domain Raman spectra. The retrieved depth-resolved Raman spectra are further optimized along axial direction using Lucy-Richardson deconvolution[23] together with the calculated point spread function of B^3-SRT technique to suppress the axial artefacts generated during the depth-resolved Raman spectra retrieval. The depth-resolved Raman spectra measured by confocal Raman spectroscopy are also smoothed using Hessian algorithm and processed with AF background subtraction in FP region using the same parameters. The Raman contributions from fat and bone of the depth-resolved Raman spectra in the two-layer tissue phantom are further estimated using non-negative least-squares regression (NNLR). The depth sctioning capability and penetration depth of the technique is further evaluated using Raman spectral contrast and deep tissue Raman signal level, respectively. The bone layer Raman spectral contrast is calculated using the Eq. (7) below based on the estimated Raman contribution of bone RC_{bone} in the fat-bone connection retion of the prepared tissue phantom (i.e., 50 µm ± 10 µm, 70 µm ± 10 µm and 90 µm ± 10 µm), while the bone layer signal level is estimated using Eq (8) associated with the Raman intensity at 960 cm^{-1} (phosphate of bone, $I_{960cm^{-1}}$) and 1445 cm^{-1} (CH_2 deformation of proteins and lipids $I_{1445cm^{-1}}$).

$$Raman\ spectral\ contrast = \frac{\max\left(RC_{bone}\right)}{\min\left(RC_{bone}\right)}. \tag{7}$$

$$Signal\ level = \frac{\max\left(I_{960cm^{-1}}\right)}{\max\left(I_{1445cm^{-1}}\right)}. \tag{8}$$

Results

We firstly investigate the Raman spectra modulation and depth retrieval ability of the B^3-SRT technique developed by measuring the depth-resolved Raman spectra of the exposed bone tissue at different axial locations (i.e., z = 100 μm and z = 150 μm) in spatial frequency domain with Δk_z ranging from 0 to 0.15 μm^{-1} as shown in **Figures 2(a)** and **2(b).** The intensity modulation of the tissue Raman spectra with respect to the Bessel beam beating frequency Δk_z can be clearly observed in both **Figures 2(a)** and **2(b)**, indicating the successful spatial information encoding and collection using the designed Bessel beam beating excitation and Bessel collection scheme. For instance, we compare the Raman intensity modulation at the representative Raman peak of bone (i.e., 960 cm^{-1} (phosphate)) with respect to Δk_z (**Figure 2(c)**)**.** The Raman intensities are normalized to the intensities at $\Delta k_z = 0$ μm^{-1} for z = 100 μm and z = 150 μm, respectively. In **Figure 2(c)**, a higher beating frequency (~ 1.5 times) of the normalized Raman intensity at 960 cm^{-1} can be observed when the bone sample is placed at z = 150 μm compared to z = 100 μm, confirming the increasing trend of Raman signal beating frequency with respect to the increase of sample depth as designed in Eq. (4). The retrieved depth-resolved Raman spectra of bone at z = 100 μm and z = 150 μm are depicted in **Figures 2(d)** and 2(**e**), respectively. The depth-resolved Raman spectra of bone tissue are accurately retrieved at z = 100 μm and z = 150 μm, proving the effectiveness of B^3-SRT technique for uncovering depth-resolved Raman information. The tissue Raman spectra retrieved at z = 100 μm and z = 150 μm are shown in **Figure 2(f)**. Representative Raman peaks (i.e., 960 cm^{-1} (phosphate), 1070 cm^{-1} (carbonate), 1250 cm^{-1} (Amide III), 1450 cm^{-1} (CH_2), and 1665 cm^{-1} (Amide I))[3] of bone tissue can be clearly observed in both tissue depths, confirming the capability of B^3-SRT technique for accurately retrieving tissue Raman spectra with axial information.

The axial resolution of the B^3-SRT technique developed has also been evaluated both theoretically and experimentally. In this study, the axial wavevector k_z of one excitation Bessel beam is fixed at 7.80 μm^{-1} (numerical aperture (NA) = 0.22), while the axial wavevector k_z' is changing from 7.80 to 7.95 μm^{-1} in 51 phase patterns for the other excitation Bessel beam, resulting the Δk_z scanning ranges of 0 to 0.15 μm^{-1} (refractive index n = 1 in air). Because $I_{Ra}(\omega, \Delta k_z)$ is an even function of Δk_z,

the actual Δk_z range for depth-resolved Raman spectra retrieval is -0.15 to 0.15 μm^{-1}. The theoretical resolution of B^3-SRT technique with such Δk_z scanning range can be calculated as 25.14 μm using Eq. (6). The real axial resolution of the designed B^3-SRT system is measured using a PMMA sheet. **Figure 3(a)** shows the depth-resolved Raman spectra of PMMA sheet measured using B^3-SRT technique without deconvolution. The representative Raman peak intensity of PMMA at 1445 cm^{-1} (indicated in blue dash line in **Figure 3(a)**) is selected for the axial resolution estimation. The Raman intensity at the edge is firstly processed by taking the first-order derivative with respect to z and then fitted by a Gaussian curve. The axial resolution of the B^3-SRT system is calculated as $\Delta_z \approx 23\ \mu m$ using the full width half maxima (FWHM) of the fitted Gaussian curve, which is close to the theoretical calculation. The lateral resolution of the B^3-SRT system can be calculated as the FWHM of the main lobe of the excitation and collection Bessel functions, $\Delta_r \approx\ 1.2\ \mu m$. The axial and lateral resolutions of the conventional confocal Raman spectroscopy under the same NA (i.e., NA = 0.22) can also be calculated as follows:$\Delta_r \approx \frac{0.56\lambda}{NA}\ \approx 2\ \mu m$,[24] and $\Delta_z \approx \frac{2\lambda}{\sqrt{2}NA^2}\ \approx 22.93\ \mu m$.[19] **Figure 3(b)** compares the theoretical axial point spread function (PSF) of confocal[25] and B^3-SRT (Eq. (8)) as well as the measured axial PSF of B^3-SRT. Overall, the developed B^3-SRT technique shows a higher lateral resolution (i.e., improved by 1.66 times) and a similar axial resolution as compared with the conventional confocal Raman spectroscopy when the same NA is used.

The deep tissue Raman measurement ability of B^3-SRT technique is demonstrated using a highly scattering two-layer tissue phantom prepared using the 50 μm thick fat tissue overlaying on the 2 mm thick bone tissue. **Figure 4(a)** shows the tomographic image of the prepared fat-bone tissue phantom captured using OCT. The prepared tissue phantom was then measured using B^3-SRT technique. **Figure 4(b)** shows the collected Raman spectra with respect to Δk_z. The intensity modulation of the Raman peaks of bone and fat tissues (e.g., 960 cm^{-1}, 1078 cm^{-1}, 1296 cm^{-1}, 1445 cm^{-1} and 1665 cm^{-1}) can be clearly observed, indicating the effective modulation of Raman signal at different tissue layers. The representative Raman peak of bone (960 cm^{-1} (phosphate)) and fat (1445 cm^{-1} (CH_2 deformation of proteins and lipids)) tissue are further selected and normalized to their maximum intensity for comparison (**Figure 4 (c)**). The Raman signal at 960 cm^{-1} which mainly comes

from the underlying bone layer in the tissue model shows a higher beating frequency in Δk_z domain compared to the Raman signal at 1445 cm^{-1} mainly originating from the fat layer, indicating the Raman signal of fat and bone layers are encoded with different beating frequencies. **Figure 4(d)** shows the depth-resolved tissue Raman spectra retrieved by B^3-SRT technique, where significant Raman spectral separation can be observed at the depth of ~ 40 – 50 µm, indicating the successful Raman spectra retrieval with accurate depth information. The retrieved Raman intensity of the representative Raman peaks of bone and fat (i.e., 960 cm^{-1} and 1445 cm^{-1}) are depicted in **Figure 4(e)**. The Raman peak of 1445 cm^{-1} mainly contributed by fat tissue exhibits in the depth ranging from 0 – 47 µm while the Raman peak of 960 cm^{-1} contributed by bone tissue is showing intense Raman signal at the depth > 47 µm, which matches the tissue tomography image measured by OCT (**Figure 4(a)**), proving the depth-resolved capability of B^3-SRT technique in Raman signal retrieval. We further compared the retrieved Raman signal at the fat and bone tissue layers with pure Raman spectra of bone and fat tissues. **Figure 4(f)** compares the mean Raman spectra of pure fat and B^3-SRT retrieved spectra at 10 µm, as well as the Raman spectra of pure bone and B^3-SRT retrieved spectra at 65 µm with ±1 standard deviation (SD) in shades. Prominent Raman peaks of fat and bone tissues are shown with a high similarity to the Raman spectra of pure fat and bone (e.g., 875 cm^{-1} (ν(C-C) stretching of hydroxyproline), 960 cm^{-1} (phosphate), 1070 cm^{-1} (carbonate), 1078 cm^{-1} (ν(C-C) of lipids), 1250 cm^{-1} (Amide III), 1296 cm^{-1} (CH_2 deformation), 1445 cm^{-1} (CH_2 deformation of proteins and lipids), 1450 cm^{-1} (CH_2), 1655 cm^{-1} (Amide I and ν(C=C) of lipids), 1665 cm^{-1} (Amide I), and 1734 cm^{-1} (C=O stretching of lipids)),[3,26] affirming the effectiveness of B^3-SRT technique developed for retrieving Raman spectra with accurate depth information in the multi-layer turbid tissues.

The in-depth analysis of the deep tissue Raman measurement performance of B^3-SRT technique developed has been further conducted by measuring the fat-bone phantoms with the three fat layer thickness (i.e., 50 µm, 70 µm, and 90 µm) and also compared with the performance of the conventional confocal Raman spectroscopy. **Figures 5 (a) and (b)** show the depth-resolved Raman spectra of fat-bone tissue phantom with fat layer thickness of 50 µm, 70 µm and 90 µm measured by B^3-SRT and confocal, respectively. Raman spectra are normalized into the total area under the curve at each depth

in the figures. The significant Raman spectra separations can be clearly observed in the depth-resolved Raman spectra retrieved by B^3-SRT at the fat-bone tissue interface of 50 μm, 70 μm and 90 μm, respectively, while the bone signal always starts to increase at the depth of ~ 40 – 60 μm in the confocal measured depth-resolved Raman spectra for all three tissue phantoms. The result shows the superior depth-selective capability of B^3-SRT technique compared to confocal Raman spectroscopy technique in the deep tissue Raman measurements of turbid samples. The depth-resolved Raman spectra are further fitted by pure bone and fat tissue Raman spectra using NNLR to quantitatively analyze the depth-resolved Raman contribution from fat and bone. **Figure 5(c)** depicts the calculated depth-resolved fat and bone Raman contribution of tissue phantoms measured by B^3-SRT and confocal Raman, respectively. A higher fat Raman contribution and the lower bone Raman contribution can be found at the first tissue layer region for B^3-SRT compared to confocal, while a higher bone Raman contribution with a lower fat Raman contribution is shown in the fitting results of B^3-SRT compared to confocal Raman spectroscopy. This indicates the better depth sectioning capability of B^3-SRT in deep tissue Raman measurements compared to confocal Raman spectroscopy.

To evaluate the depth selective capability in deep tissue Raman measurements of the B^3-SRT technique developed, we further calculated the bone layer Raman spectral contrasts using the NNLR fitting results of B^3-SRT and confocal, respectively. The Raman spectral contrasts are calculated as the maximum of the bone Raman contribution divided by the minimum bone Raman contribution in the tissue connection region (i.e., 50 μm ± 10 μm, 70 μm ± 10 μm and 90 μm ± 10 μm) as indicated in Materials and Methods. **Figure 6(a)** shows the calculated mean bone layer contrasts of B^3-SRT and confocal in a bar chart with ±1 SD. Compared to confocal Raman spectroscopy, B^3-SRT shows significantly higher bone layer Raman spectral contrasts ($p<0.05$) in all the three tissue phantoms (50 μm: B^3-SRT: 2.58 ± 0.68, confocal: 1.79 ± 0.06, 70 μm: B^3-SRT: 3.36 ± 0.56, confocal: 1.41 ± 0.03, and 90 μm: B^3-SRT: 3.12 ± 0.49, confocal: 1.2 ± 0.02), proving the superior spectral contrast of B^3-SRT compared to confocal in deep tissue Raman measurements. To compare the penetration capability in deep tissue Raman measurements, the bone layer Raman signal levels of three tissue phantoms measured by B^3-SRT and confocal Raman spectroscopy are also estimated using the maximum Raman

intensity of the bone at 960 cm^{-1} in the second tissue layer divided by the maximum Raman intensity of fat at 1445 cm^{-1} in the first tissue layer. **Figure 6(b)** displays the calculated mean bone layer signal levels of B^3-SRT and confocal in a bar chart with ±1 SD. Compared to confocal Raman spectroscopy, B^3-SRT also provides significantly higher bone layer signal levels ($p<0.05$) in all the three tissue phantoms (50 μm: B^3-SRT: 0.96 ± 0.15, confocal: 0.48 ± 0.01, 70 μm: B^3-SRT: 1.86 ± 0.62, confocal: 0.54 ± 0.02, and 90 μm: B^3-SRT: 1.06 ± 0.18, confocal: 0.29 ± 0.01). The above results further confirm the ability of B^3-SRT technique for enhancing the penetration depth in deep tissue Raman measurements as compared with conventional confocal Raman spectroscopy.

Discussion

Measuring Raman spectra from deep turbid tissues with high depth-selectivity is challenging in biomedical Raman spectroscopy. Due to the inherently strong scattering properties of the turbid tissue medium, most of current Raman spectroscopy technique could only access the surface/sub-surface area with limited axial resolution.[8] Conventional confocal Raman spectroscopy with Gaussian excitation and collection suffers from the focal degradation and out-of-focus Raman signal contamination in deep tissue Raman measurements, while the newly developed deep Raman spectroscopy techniques (e.g., SORS and KRS, etc.) may only provide the limited axial resolution in millimetre scales.[3,8,11–14] In this study, we have presented a novel Bessel beam beating-based spontaneous Raman tomography (B^3-SRT) technique to achieve the high-contrast deep tissue Raman measurements. The depth information of the Raman spectra from different tissue layers is uniquely encoded with optical beating frequencies designed in B^3-SRT technique. Further, an innovative Bessel-shaped collection function is realized to specifically collect the modulated Raman signal along the excitation Bessel beam simultaneously for effectively suppressing the Raman interference originating from the Bessel side lobes (**Figure 1(a)**). The encoded depth-information by beating frequencies (Δk_z) are rapidly decoded by implementing IFFT.

We have systematically derived and analyzed the working principle of modulation and collection of Bessel beam beating-modulated Raman conceived in B^3-SRT, and also demonstrated the superior performance of B^3-SRT experimentally. The depth-resolved Raman spectra measurement capability of B^3-SRT technique was firstly demonstrated by measuring the bone tissue layer at the two axial locations (e.g., z = 100 μm and z = 150 μm). Collected Raman signals of bone tissue at two axial locations show obviously different beating frequencies with respect to Δk_z (**Figures 2 (a)-(c)**), showing the distinctive encoding of Raman signals along axial direction using B^3-SRT technique developed. By comparing the example of Raman intensity variations at 960 cm^{-1}, we can observe that the Raman signal measured at z = 150 μm has a ~ 1.5 times higher beating frequency compared to the Raman signal measured at z = 100 μm, which agrees with our design as predicted in Eq. (4). The depth-resolved Raman spectra are accurately retrieved using IFFT, where both the depth and Raman spectral information are accurately recovered, substantiating the depth and biomolecular information sensitivity of B^3-SRT technique.

The spatial resolution has been calculated and compared with the performance of B^3-SRT technique developed. The axial resolution of the B^3-SRT system developed was measured to be 23 μm (close to the theoretical value of 25.14 μm), which is similar to the conventional confocal Raman spectroscopy under the same NA ($\Delta_z \approx 22.93\mu m$, NA = 0.22) (**Figure 3(b)**). Attributing to the unique light beam-narrowing property of Bessel beam in the lateral direction,[19] the theoretical lateral resolution of B^3-SRT is ~1.66 times smaller compared to confocal Raman spectroscopy. Different from current deep Raman spectroscopy techniques (SORS and KRS) developed based on photon migration theory which only has a limited axial resolution in mm scale due to the stochastics of photon scattering processes,[8] B^3-SRT technique developed is detecting tissue Raman spectra excited by the Bessel beam beatings with specific spatial information encoding in micrometre scales, thereby providing more accurate spatial resolution in axial direction.

The deep tissue Raman measurement ability of B^3-SRT technique has been further assessed using a strong scattering two-layered fat-bone tissue phantom (**Figure 4(a)**). The Raman signal from fat and bone layers are successfully modulated by the excitation Bessel beam beatings with significantly

different beating frequencies in the Δk_z domain (**Figures 4(b) and 4(c)**), and the depth-resolved Raman spectra can be retrieved with accurate depth information, showing the effectiveness of B^3-SRT for depth-resolved Raman spectra retrieval in turbid tissue without a need of mechanical axial-scan. The retrieved tissue Raman spectra are further compared with pure tissue Raman spectra of bone and fat tissue, where the representative fat and bone Raman peaks are accurately recovered, confirming the feasibility of B^3-SRT technique developed for accurate depth-resolved Raman spectra measurement in multi-layered tissue samples. Meanwhile, the calculated Raman contributions of bone and fat along axial direction using NNLR further show a clear separation between the fat and bone layer at different depths by B^3-SRT technique in **Figure 5(c),** confirming the superior deep tissue Raman spectroscopy retrieval capability of B^3-SRT compared to confocal Raman spectroscopy.

We further analyze the deep tissue Raman measurements of B^3-SRT technique and compared with the confocal Raman spectroscopy by measuring a set of fat-bone tissue phantoms prepared with the fat layer thickness of 50 μm, 70 μm and 90 μm, respectively. Due to the effective spatial information encodings by using the Bessel beam beatings in the excitation laser, the unmodulated random scattering Raman signal from out-of-focus region can be effectively eliminated in deep tissue Raman measurements in B^3-SRT technique. This benefits the clear separation of the fat and bone Raman spectral features at the tissue connection interface at the depth of 50 μm, 70 μm and 90 μm, respectively, in B^3-SRT (**Figure 5(a)**), while the depth-resolved spectra measured by confocal Raman spectroscopy show a significant interference between the bone and fat particularly in the thicker fat tissues (**Figure 5(b)**). Again, this validates that B^3-SRT technique has an enhanced depth sectioning capability in deep tissue Raman spectra measurements compared to conventional confocal Raman spectroscopy.

We have further examined the depth sectioning capability and penetration depth of B^3-SRT technique in deep Raman measurement. The deep tissue Raman spectral contrast and signal level are mainly affected by the tissue scatterings which could introduce out-of-focus Raman signal as well as the signal level decreasing when the measurement depth in tissue increases. The unique axial modulation of excitation beam in B^3-SRT can effectively discriminate the Raman signals from different depths. Compared to confocal Raman spectroscopy, B^3-SRT provides ~1.44-, 2.38- and 2.6- fold

improvement in bone layer Raman spectral contrast in the two-layer tissue phantoms with the fat layer thickness of 50 μm, 70 μm and 90 μm, respectively (**Figure 6(a)**), confirming the better scattering photon rejection capability of B^3-SRT technique in highly scattering bio-tissue measurements. Attributing to its unique self-reconstruction property of the Bessel beam used,[19,27] deep tissue layer Raman signal levels measured using B^3-SRT technique show ~2-, 3.4- and 3.66-fold improvement compared to confocal Raman spectroscopy in measuring the two-layer tissue phantoms with the fat layer thickness of 50 μm, 70 μm and 90 μm, respectively (**Figure 6(b)**), affirming the superior penetration depth in deep tissue Raman spectroscopy by using Bessel beam excitation.

One notes that compared to the conventional confocal Raman spectroscopy with focused Gaussian beam excitation, the single mode excitation laser power in B^3-SRT technique is spread along the axial axis (~ 200 μm in our study) for deep Raman spectroscopy measurements, which offers the advantage of very low risk of photodamage to the samples due to a much reduced power density rendered in tissue. In our study, the excitation laser power used is ~80 mW on the sample, which is much lower than the commonly used excitation power (~150 mW with Gaussian excitation) in SORS[3] for deep tissue Raman spectroscopy. To further improve the tissue Raman measurement depth and spatial resolution through increasing the Bessel needle beam length and the broader scanning range of Δk_z, we could utilize a higher single mode laser excitation power (e.g., ~150 mW when commercially available) without photodamaging tissue samples in B^3-SRT technique, thus the axial resolution of B^3-SRT may achieve up to ~ 6 μm if using a 20× objectives (NA = 0.5) with millimeter scale penetration depth in deep tissue Raman characterization.

In summary, we have developed a unique B^3-SRT technique that is enabled by generating the Bessel beam beatings for depth-resolved deep tissue Raman measurements without mechanical z-scan. With the advantages of high Raman spectral contrast, deep penetration depth, high axial resolution, and low risk of tissue photodamage due to the low power density used as demonstrated in this work, we expect that B^3-SRT technique has promise to significantly facilitate high contrast depth-resolved deep tissue Raman measurements in biomedical systems.

Acknowledgements

This work was supported in part by the Academic Research Fund (AcRF) -Tier 2 (A-8000117-01-00) and Tier 1 (WBS R-397-000-326-114, WBS R-397-000-334-114, WBS R-397-000-371-114, and WBS R-397-000-378-114) from the Ministry of Education (MOE), Merlion Fund (WBS R-397-000-356-133), and the National Medical Research Council (NMRC) (R397-000-384-213), Singapore.

Contributions

Z.H and C S. conceived the concept. C.S. designed and constructed the instrument, and performed experiments with data analysis. L.G helped with data analysis; Z.H. and C.S. wrote the manuscript, and Z.H. finalized the manuscript.

Data availability

The data acquired for this study are available from the corresponding author upon reasonable request.

Conflict of interest

The authors declare no competing interests.

Supplementary information

1. Mathematics for Bessel beam beating-based spontaneous Raman tomography (B^3-SRT)
2. Collection function of Bessel beam beating-based spontaneous Raman tomography (B^3-SRT)
3. Hessian Denoising for the spatial frequency domain Raman spectral mapping

Reference

1 Raman C V., Krishnan KS. A New Type of Secondary Radiation. *Nature* 1928; **121**: 501–502.

2 Heng HPS, Shu C, Zheng W, Lin K, Huang Z. Advances in real-time fiber-optic Raman spectroscopy for early cancer diagnosis: Pushing the frontier into clinical endoscopic applications. *Transl Biophotonics* 2021; **3**: e202000018.

3 Shu C, Chen K, Lynch M, Maher JR, Awad HA, Berger AJ. Spatially offset Raman spectroscopy for in vivo bone strength prediction. *Biomed Opt Express* 2018; **9**: 4781–4791.

4 Shu C, Yan H, Zheng W, Lin K, James A, Selvarajan S *et al.* Deep Learning-Guided Fiberoptic Raman Spectroscopy Enables Real-Time In Vivo Diagnosis and Assessment of Nasopharyngeal Carcinoma and Post-treatment Efficacy during Endoscopy. *Anal Chem* 2021; **93**: 10898–10906.

5 Lin K, Zheng W, Lim CM, Huang Z. Real-time In vivo Diagnosis of Nasopharyngeal Carcinoma Using Rapid Fiber-Optic Raman Spectroscopy. *Theranostics* 2017; **7**: 3517–3526.

6 Huang Z, McWilliams A, Lui H, McLean DI, Lam S, Zeng H. Near-infrared Raman spectroscopy for optical diagnosis of lung cancer. *Int J Cancer* 2003; **107**: 1047–1052.

7 Shu C, Zheng W, Lin K, Lim C, Huang Z. Label-Free Follow-Up Surveying of Post-Treatment Efficacy and Recurrence in Nasopharyngeal Carcinoma Patients with Fiberoptic Raman Endoscopy. *Anal Chem* 2021; **93**: 2053–2061.

8 Matousek P, Stone N. Emerging concepts in deep Raman spectroscopy of biological tissue. *Analyst* 2009; **134**: 1058–1066.

9 Shu C, Zheng W, Wang Z, Yu C, Huang Z. Development and characterization of a disposable submillimeter fiber optic Raman needle probe for enhancing real-time in vivo deep tissue and biofluids Raman measurements. *Opt Lett* 2021; **46**: 5197–5200.

10 Giridhar G, Manepalli RRKN, Apparao G. Chapter 7 - Confocal Raman Spectroscopy. In: Thomas S, Thomas R, Zachariah AK, Mishra RKBT-SM for NC (eds). *Micro and Nano*

Technologies. Elsevier, 2017, pp 141–161.

11 Clendenon SG, Young PA, Ferkowicz M, Phillips C, Dunn KW. Deep tissue fluorescent imaging in scattering specimens using confocal microscopy. *Microsc Microanal* 2011; **17**: 614–617.

12 Schmitt JM, Knüttel A, Yadlowsky M. Confocal microscopy in turbid media. *J Opt Soc Am A* 1994; **11**: 2226–2235.

13 Schmitt JM, Ben-Letaief K. Efficient Monte Carlo simulation of confocal microscopy in biological tissue. *J Opt Soc Am A* 1996; **13**: 952–961.

14 Freebody NA, Vaughan AS, Macdonald AM. On optical depth profiling using confocal Raman spectroscopy. *Anal Bioanal Chem* 2010; **396**: 2813–2823.

15 Matousek P, Clark IP, Draper ERC, Morris MD, Goodship AE, Everall N *et al.* Subsurface Probing in Diffusely Scattering Media Using Spatially Offset Raman Spectroscopy. *Appl Spectrosc* 2005; **59**: 393–400.

16 Draper ERC, Morris MD, Camacho NP, Matousek P, Towrie M, Parker AW *et al.* Novel Assessment of Bone Using Time-Resolved Transcutaneous Raman Spectroscopy. *J Bone Miner Res* 2005; **20**: 1968–1972.

17 Berry ME, McCabe SM, Sloan-Dennison S, Laing S, Shand NC, Graham D *et al.* Tomographic Imaging and Localization of Nanoparticles in Tissue Using Surface-Enhanced Spatially Offset Raman Spectroscopy. *ACS Appl Mater Interfaces* 2022; **14**: 31613–31624.

18 Maher JR, Inzana JA, Awad HA, Berger AJ. Overconstrained library-based fitting method reveals age- and disease-related differences in transcutaneous Raman spectra of murine bones. *J Biomed Opt* 2013; **18**: 1–12.

19 Gong L, Lin S, Huang Z. Stimulated Raman Scattering Tomography Enables Label-Free Volumetric Deep Tissue Imaging. *Laser Photonics Rev* 2021; **15**. doi:10.1002/LPOR.202100069.

20 Shimojo Y, Nishimura T, Hazama H, Ozawa T, Awazu K. Measurement of absorption and reduced scattering coefficients in Asian human epidermis, dermis, and subcutaneous fat tissues in the 400- to 1100-nm wavelength range for optical penetration depth and energy deposition analysis. *J Biomed Opt* 2020; **25**: 45002.

21 Liu Y, Wang Y, Qian Z, Zhao J, Cao X, Li W. Monitoring the reduced scattering coefficient of bone tissues on the trajectory of pedicle screw placement using near-infrared spectroscopy. *J Biomed Opt* 2014; **19**: 117002.

22 Huang X, Fan J, Li L, Liu H, Wu R, Wu Y *et al.* Fast, long-term, super-resolution imaging with Hessian structured illumination microscopy. *Nat Biotechnol* 2018; **36**: 451–459.

23 Richardson WH. Bayesian-Based Iterative Method of Image Restoration*. *J Opt Soc Am* 1972; **62**: 55–59.

24 Boudoux C. *Fundamentals of biomedical optics : from light interactions with cells to complex imaging systems*. 1st ed. 2016.

25 Richards B, Wolf E, Gabor D. Electromagnetic diffraction in optical systems, II. Structure of the image field in an aplanatic system. *Proc R Soc London Ser A Math Phys Sci* 1959; **253**: 358–379.

26 Movasaghi Z, Rehman S, Rehman I. Raman Spectroscopy of Biological Tissues. *Appl Spectrosc Rev* 2007; **42**: 493–541.

27 Fahrbach FO, Simon P, Rohrbach A. Microscopy with self-reconstructing beams. *Nat Photonics* 2010; **4**: 780–785.

Figure Captions

Figure 1. (a) Working principle of the Bessel beam beatings excitation and Bessel collection scheme in B^3-SRT technique. (b) The procedure of retrieving depth-resolved Raman spectra using B^3-SRT technique. (c) Schematic of B^3-SRT system. Abbreviations: SLM: spatial light modulator, L: lens, BP: band-pass filter, DM: dichroic mirror, LP: long-pass filter, MMF: multimode fiber, CCD: charge-coupled device.

Figure 2. The bone tissue Raman spectral image acquired in Δk_z domain when the sample is placed at the axial location of (a) z = 100 μm and (b) z = 150 μm, respectively. (c) Comparison of Raman intensity at 960 cm^{-1} with respect to Δk_z measured using B^3-SRT technique when the bone tissue is placed at the axial locations of z = 100 μm and z = 150 μm (The Raman intensities are normalized to the intensity at $\Delta k_z = 0\ \mu m^{-1}$). The retrieved depth-resolved Raman spectra by B^3-SRT technique when the bone tissue is placed at the axial locations of (d) z = 100 μm and (e) z = 150 μm, respectively. (f) Raman spectra of the bone tissue retrieved by B^3-SRT technique at the axial locations of z = 100 μm and z = 150 μm, respectively.

Figure 3. (a) Depth-resolved Raman spectra of PMMA sheet retrieved by B^3-SRT technique. (b) Comparison among the measured axial point spread function (PSF) of B^3-SRT, the theoretical PSF of B^3-SRT, and the theoretical axial PSF of confocal microscopy.

Figure 4. (a) The fat-bone tissue phantom with the fat tissue thickness of 50 μm overlaid on the bone tissue measured by optical coherence tomography (Scale bar: 50 μm). (b) The fat-bone tissue Raman spectral image using B^3-SRT technique in Δk_z domain. (c) Comparison of tissue Raman intensity variations with respect to Δk_z between the Raman peaks of 960 cm^{-1} and 1445 cm^{-1}. Both Raman intensities are normalized to the intensity at $\Delta k_z = 0\ \mu m^{-1}$. (d) Depth-resolved fat-bone tissue Raman spectra retrieved by B^3-SRT technique. (e) Example of the Raman peak (960 cm^{-1} and 1445 cm^{-1}) intensity profiles along the depth retrieved by B^3-SRT technique. (f) Comparison between the mean tissue Raman spectra of the pure fat tissue measured ???and the Raman spectra retrieved by B^3-SRT

technique at z = 10 μm as well as between the mean tissue Raman spectra of the bone tissue measured and the Raman spectra retrieved by B^3-SRT technique at z = 65 μm, with ±1 standard deviation (SD) in shades.

Figure 5. (a) Depth-resolved Raman spectra of tissue phantom retrieved by B^3-SRT technique with the fat layer thickness of 50 μm, 70 μm and 90 μm, respectively. (b) Depth-resolved Raman spectra of tissue phantom measured by confocal Raman spectroscopy with the fat layer thickness of 50 μm, 70 μm and 90 μm, respectively. (c) Calculated contributions of bone and fat tissue Raman signals in the fat-bone tissue phantom using NNLR for B^3-SRT technique and confocal Raman spectroscopy with the fat layer thickness of 50 μm, 70 μm and 90 μm, respectively.

Figure 6. (a) Comparison of the bone layer Raman spectral contrasts between B^3-SRT technique and confocal Raman spectroscopy calculated using the maximum Raman contribution of the bone divided by the minimum in the tissue connection region (i.e., 50 μm ± 10 μm, 70 μm ± 10 μm and 90 μm ± 10 μm) in a bar chart with ±1 SD. (b) Comparison of the bone layer Raman signal levels calculated by using the maximum Raman intensity at 960 cm^{-1} divided by the Raman peak at 1445 cm^{-1} between B^3-SRT technique and confocal Raman spectroscopy in a bar chart with ±1 SD.

Figure 1

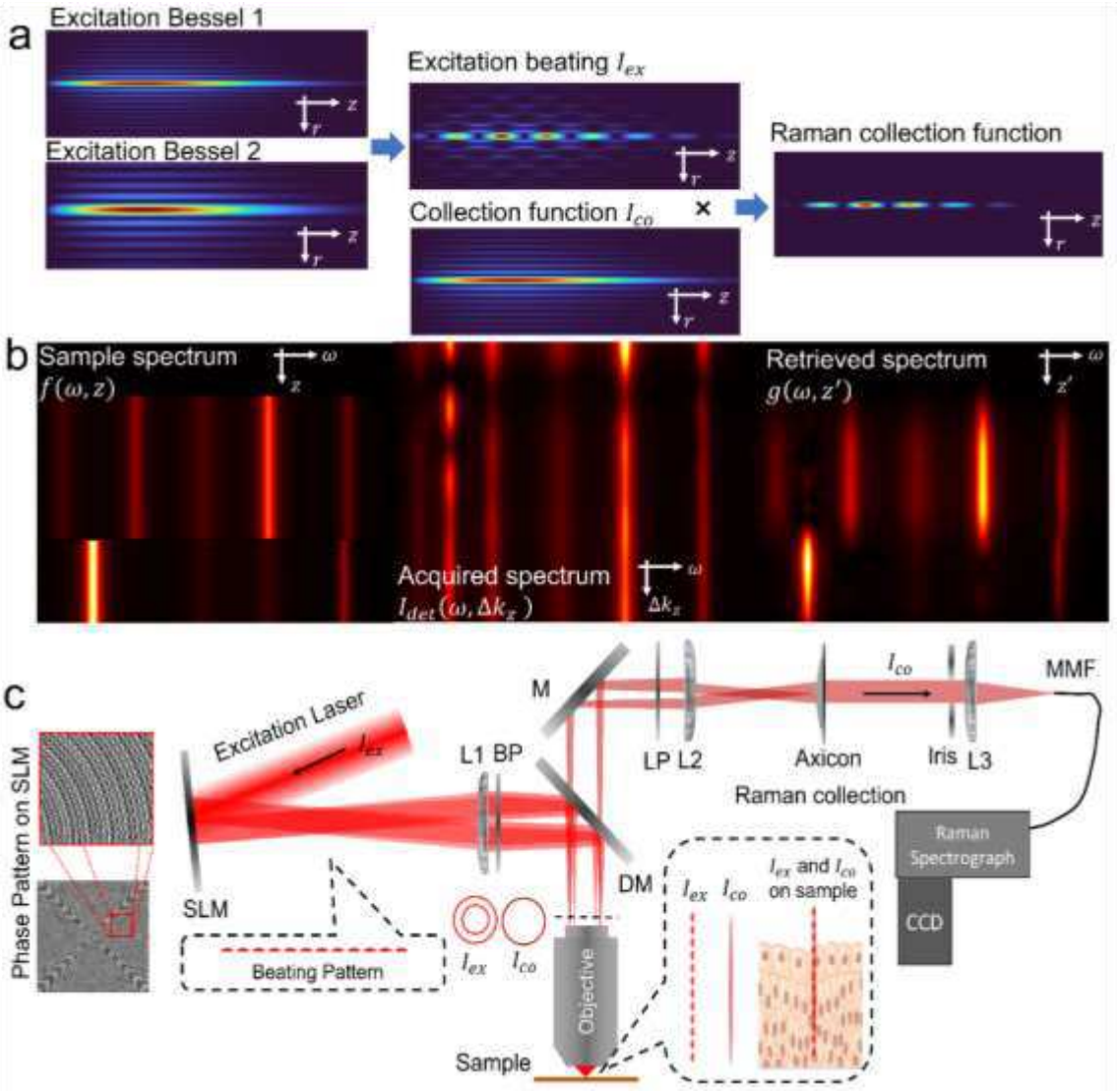
a
Excitation Bessel 1
Excitation Bessel 2
Excitation beating I_{ex}
Collection function I_{co}
Raman collection function
b
Sample spectrum
$f(\omega, z)$
Retrieved spectrum
$g(\omega, z')$
Acquired spectrum
$I_{det}(\omega, \Delta k_z)$
c
Phase Pattern on SLM
Excitation Laser
I_{ex}
SLM
Beating Pattern
L1 BP
M
LP L2
Axicon
I_{co}
Iris L3
MMF
Raman collection
DM
I_{ex} and I_{co} on sample
Raman Spectrograph
CCD
Objective
Sample

Figure 2

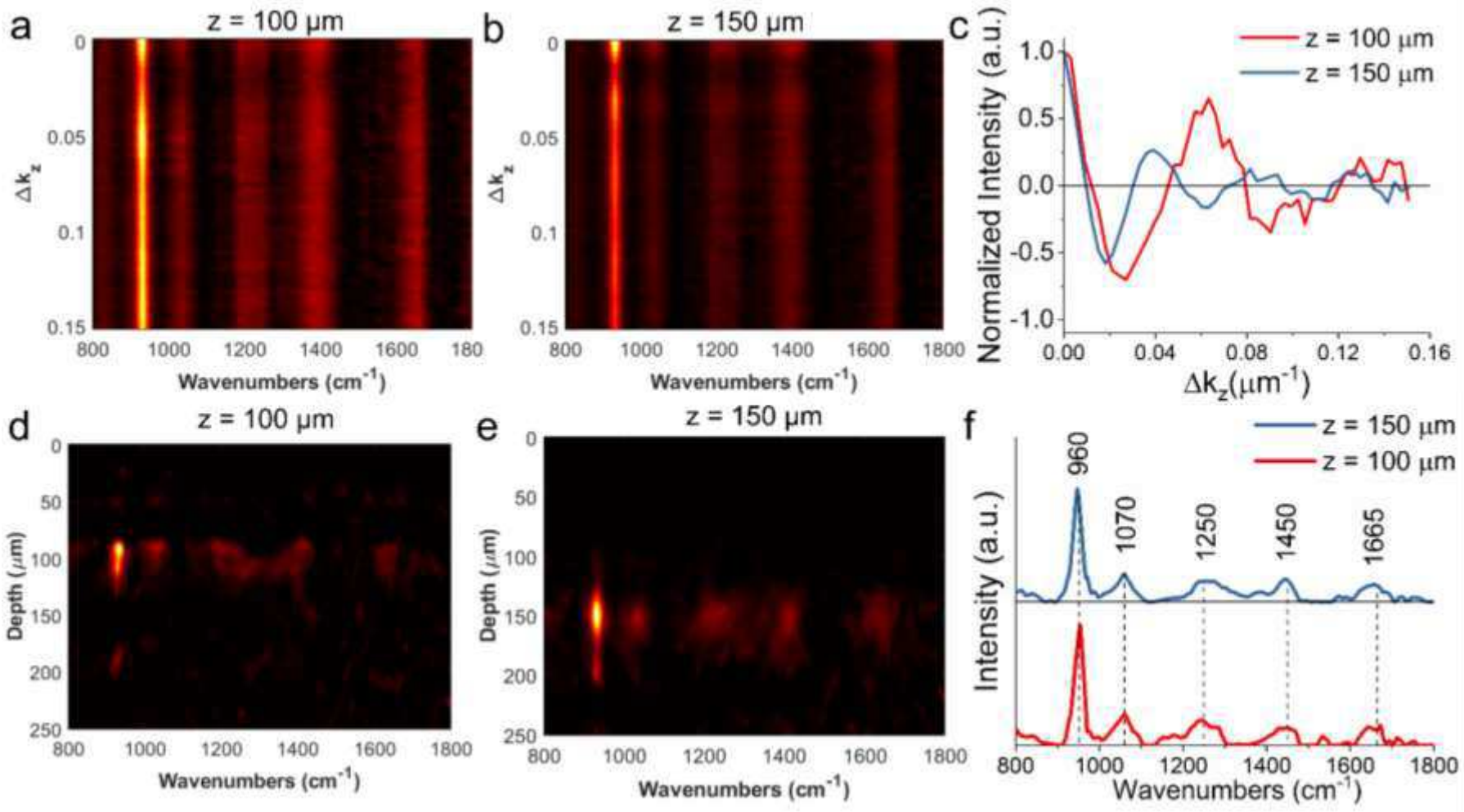
a
z = 100 μm
b
z = 150 μm
c
z = 100 μm
z = 150 μm
Normalized Intensity (a.u.)
Δk_z(μm^-1)
Δk_z
Wavenumbers (cm^-1)
d
z = 100 μm
e
z = 150 μm
Depth (μm)
f
z = 150 μm
z = 100 μm
960
1070
1250
1450
1665
Intensity (a.u.)

Figure 3

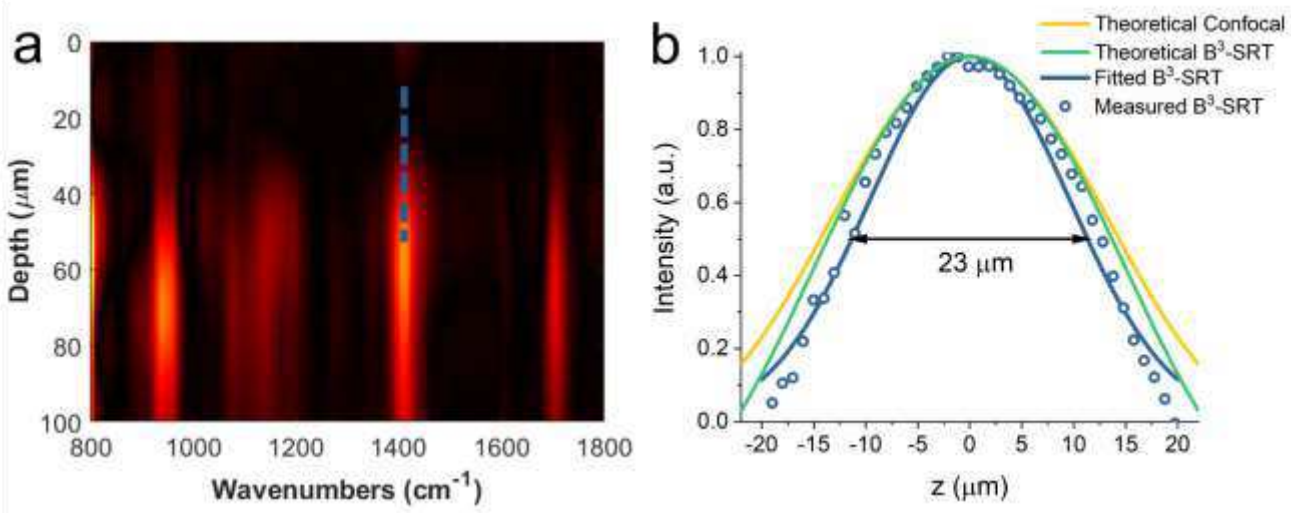
a
Depth (μm)
0
20
40
60
80
100
800
1000
1200
1400
1600
1800
Wavenumbers (cm-1)
b
Intensity (a.u.)
1.0
0.8
0.6
0.4
0.2
0.0
-20
-15
-10
-5
0
5
10
15
20
z (μm)
23 μm
Theoretical Confocal
Theoretical B3-SRT
Fitted B3-SRT
Measured B3-SRT

Figure 4

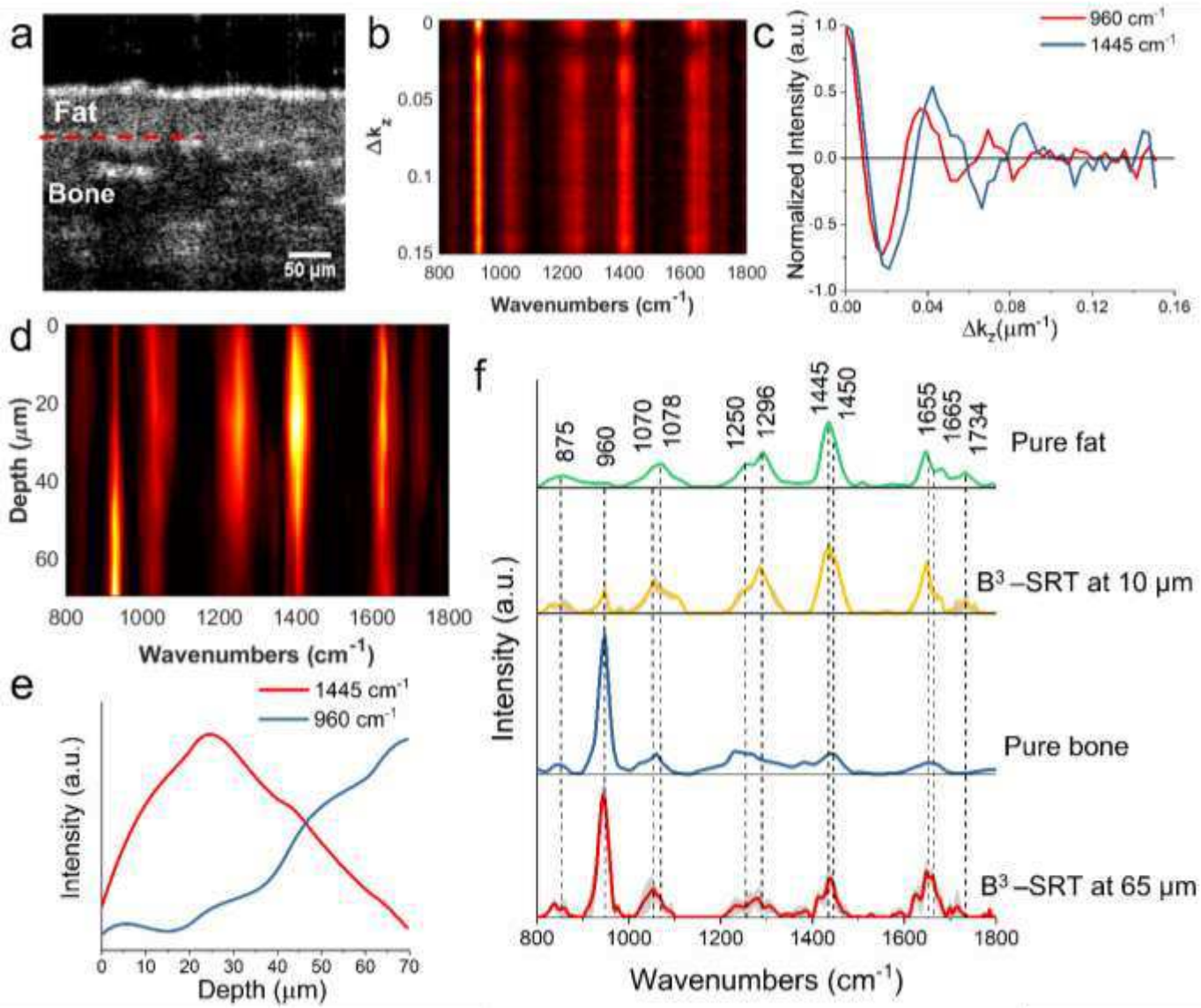
a
Fat
Bone
50 μm
b
Δk_z
Wavenumbers (cm^-1)
c
960 cm^-1
1445 cm^-1
Normalized Intensity (a.u.)
Δk_z(μm^-1)
d
Depth (μm)
Wavenumbers (cm^-1)
e
1445 cm^-1
960 cm^-1
Intensity (a.u.)
Depth (μm)
f
875
960
1070
1078
1250
1296
1445
1450
1655
1665
1734
Pure fat
B3 –SRT at 10 μm
Pure bone
B3 –SRT at 65 μm
Intensity (a.u.)
Wavenumbers (cm^-1)

Figure 5

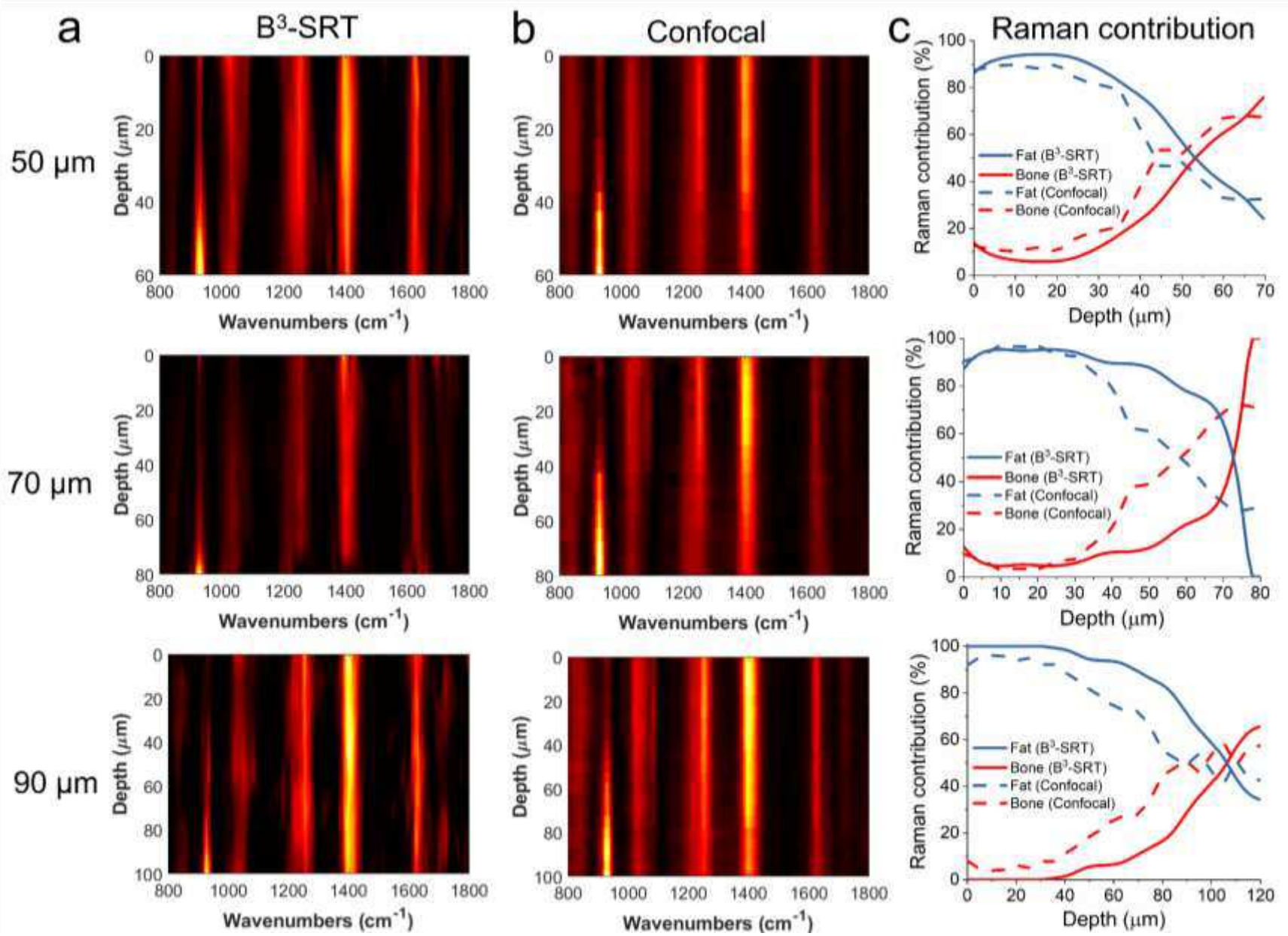
a
B3-SRT
b
Confocal
c
Raman contribution
50 μm
70 μm
90 μm
Depth (μm)
Wavenumbers (cm-1)
Raman contribution (%)
Depth (μm)
Fat (B3-SRT)
Bone (B3-SRT)
Fat (Confocal)
Bone (Confocal)

Figure 6

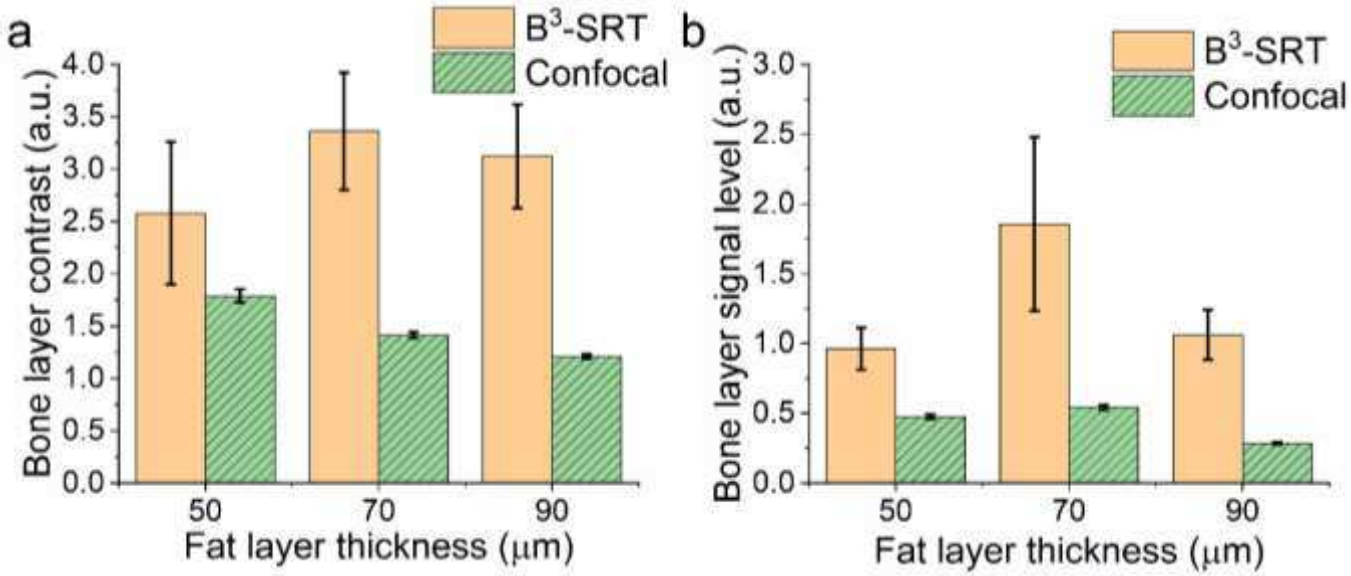
a
B3-SRT
Confocal
Bone layer contrast (a.u.)
4.0
3.5
3.0
2.5
2.0
1.5
1.0
0.5
0.0
50
70
90
Fat layer thickness (μm)
b
B3-SRT
Confocal
Bone layer signal level (a.u.)
3.0
2.5
2.0
1.5
1.0
0.5
0.0
50
70
90
Fat layer thickness (μm)

Supplementary Files

This is a list of supplementary files associated with this preprint. Click to download.

- SIDeepRamanProfHuang.docx